

# Scattering Spectroscopy of Plasmonic Janus Particles

Felix H. Patzschke, A. Markus Anton and \*Frank Cichos

## Abstract

Plasmonic Janus particles consist of dielectric core particles with a thin metallic cap on one side and are widely used in active matter research. [1] The plasmonic cap enhances optical scattering and absorption, allowing for self-propulsion through temperature gradients as well as efficient trapping and tracking. [2, 3] The asymmetry of such a particle gives rise to surface plasmon modes whose excitation is sensitive to the angle at which the particle is illuminated. Even though the angle of illumination strongly influences the particle's scattering response, the optical properties of such metallic caps have hardly been investigated.

We probe the light scattering of individual micrometre-sized, spherical, Au-coated Janus particles by means of Selective Illumination Multiplexed Fourier Plane Spectroscopy. This novel method allows us to explore microparticles' scattering characteristics resolved for wavelength, angle of illumination and scattering angle.

In addition, we supplement our experimental results with finite-element simulations and correlate spectral markers to orientation-dependent surface plasmon modes. This additional information on the correlation of angular and spectral information could pave the way for new methods of orientation detection. They also shed new light on the interaction of such spherically capped particles with light inducing forces and torques. [4, 5]

## Introduction

Janus particles (JPs) with a plasmonically active cap are a widely-used tool in active matter research: Through the absorption of visible light, the cap can be heated efficiently. In conjunction with the anisotropy of the particle, this facilitates directed self-propulsion. Meanwhile, the enhanced optical scattering of the cap leads to good visibility in microscopy, particularly in the dark field, which, in turn, allows for accurate tracking of the motile particles.

As widely applicable as these particles' light-matter interactions (LMIs) may be, they are certainly not trivial: The length scales of the surface curvature are in the same order of magnitude as the wavelengths of light in the interaction, such that approximations along the lines of ray optics or dipole scattering are invalid. In addition, the asymmetry of the particles leads to orientation-dependency of the LMI. These orientation-dependencies may manifest in counter-intuitive ways: Some purely numerical studies suggest that plasmonic JPs can stably rotate, powered by a linearly polarized light field. [4, 5]

To our knowledge, this manner of LMIs has not yet been systematically studied. Orientation-dependent scattering studies of plasmonic nanostructures<sup>1</sup> have been performed, [6] but neither on JPs nor with a capacity for spectral resolution beyond RGB-decomposition. Moreover, no regard was given to the angular distribution of the scattered light.<sup>2</sup>

We present an experimental method, which we use to study the LMI of plasmonic JPs consisting of

a spherical polystyrene (PS) particle, 1  $\mu\text{m}$  in diameter, with a 50 nm thick gold layer as the cap. We resolve the intensity of scattered light for wavelength and scattering angle. Though the theory of Mie [7] only makes predictions for maximally symmetric particles, it serves well as reference in the characterization of the LMI of plasmonic JPs. We complement the measurement results with numerical simulations and find a good match between both methods' results. Through the analysis of the simulation results, we correlate peaks in the scattering spectra to orientation-dependent surface plasmon modes.

## Definitions

The geometry of the system of interest is as follows: A polystyrene (PS) sphere ( $r = 0.5 \mu\text{m}$ ), centered at the origin, represents the core of the JP. The gold cap is modelled as half of an ellipsoidal shell (semi major axis: 0.55  $\mu\text{m}$ , semi minor axes: 0.51  $\mu\text{m}$ ) around the PS sphere. It is cut off in the plane of the minor axes, its major axis coincides with the symmetry axis of the JP. This construct is surrounded by an ambient medium with a constant, real-valued refractive index.

The orientation of the system is characterised by the angles between three unit vectors;

$\hat{z}$ , the symmetry axis of the particle, oriented such that the Au cap lies in the positive and the PS side in the negative  $z$ -direction,

$\hat{k}$ , the propagation direction of the incident light,

<sup>1</sup>specifically, Au nano-rods and -triangles, sized between 100 and 150 nm

<sup>2</sup>which on such small objects isn't necessary - the angular distributions look pretty much the same - but for larger particles, the differences in the shapes of the Mie plots can lead to drastic differences between the "true" scattering spectra and the measured ones.

with respect to which scattering angles are defined and

$\hat{o}$ , the "forward" direction along the optical axis, equivalent to the central axis of the objective's collection cone.

In terms of these, the out-of-plane orientation of the JP is defined as  $\alpha := \angle(\hat{o}, \hat{z})$ . Similarly, we define the illumination angle  $\zeta := \angle(\hat{k}, \hat{z})$ , which, in this model, is the only orientation parameter needed to define the light-matter interaction of the JP.

Scattering angles are defined for each plane-wave contribution to the scattered field: Let that contribution have a propagation direction  $\hat{k}'$ . Then,  $\theta := \angle(\hat{k}', \hat{k})$  is the polar component of the scattering angle. Additionally, there is an azimuthal component  $\phi$ , the choice of reference point for which being somewhat arbitrary. In the following, it will be chosen such that if  $\hat{k}'$  lies in the  $(\hat{k}, \hat{z})$  plane, then  $\phi = 0$ .

These definitions are illustrated in [Figure].

## Methods

### Finite-Element Simulations

The finite-element simulations were performed in COMSOL Multiphysics 6.1. The model geometry, based on models E1 and E2 from [5], was defined in particle-coordinates, i.e.  $\hat{z}$  coincides with the  $z$ -axis.

As parameters, the simulation takes in the *illumination angle*,

$$\zeta := \angle(\hat{z}, \hat{k}) ,$$

and the incident (vacuum-) wavelength  $\lambda$ .

Numerically, the properties of the scattered light field were obtained using COMSOL Multiphysics. [Intro to the geometric model. The COMSOL model is qualitatively the same as in [5]. ] The surrounding medium was modelled with a refractive index of 1.51.

Given a plane wave

$$\vec{E}_{\text{incident}}(\vec{x}, t) = \vec{E}_0 \cdot \exp(i \vec{k} \cdot \vec{x} - i \omega t)$$

as the incident field, the solver produced a point-wise solution

$$\vec{E}(\vec{x}, t) = \vec{E}_{\text{incident}}(\vec{x}, t) + \vec{E}_{\text{sca}}(\vec{x}, t)$$

to Maxwell's field equations on the defined geometry, where  $\vec{E}_{\text{sca}}(\vec{x}, t)$  is the scattered field.

The scattering cross-section of the particle was calculated from the scattered field as

$$\sigma_{\text{sca}} = \frac{2\mu_0\mu_r}{\|\vec{E}_0\|^2} \cdot \oint_{\partial V} \langle \vec{S}_{\text{sca}} \rangle_t \cdot d\vec{A} ,$$

where  $\vec{S}_{\text{sca}}$  is the Poynting vector of the scattered field and  $\langle \cdot \rangle_t$  denotes the time average.

<sup>3</sup>TO DO: serial number

[Explanation on how the scattering intensity is resolved for  $\hat{k}$ ] The scattered field can, according to Fourier's theorem, be decomposed into plane-wave components

$$d\vec{E}(\vec{x}, t) := \vec{E}(\vec{k}) \cdot \exp(i \vec{k} \cdot \vec{x} - i \omega t) d^3k ,$$

such that  $\vec{E}_{\text{sca}} = \iiint_{\mathbb{R}^3} d\vec{E}$ . The amplitudes  $\vec{E}(\vec{k})$  of the components are given by the Fourier transform of  $\vec{E}(\vec{x}, t)$ . The intensities of the components are given by

$$d\mathcal{I}(\vec{k}) = \frac{\langle \|\vec{E}(\vec{k})\|^2 \rangle_t}{2\mu_0\mu_r} d^3k .$$

With any fixed wavelength  $\lambda$ , the wavevectors are conveniently expressed as  $\vec{k} = 2\pi\lambda^{-1} \cdot \hat{k}$ , where  $\hat{k} \in \mathcal{S}^2$  is a unit vector. One obtains the spectral and angular distribution of scattered light,  $d\mathcal{I}(\lambda, \Omega)$ , where  $\Omega$  parametrizes the 2-sphere.

## Experiments

### Sample Preparation

The JPs were produced by [cite production from Nic's work] and consist of spherical PS beads, coated with a layer of gold, 50 nm thick on average, on one side, with a 5 nm thick layer of chromium as a binding agent in between. A 30  $\mu\text{l}$  droplet was placed on a cover slip and the JPs in solution were left to sediment for 10 minutes. Afterwards, the solvent was blown off using nitrogen gas, leaving the remaining JPs stuck on the coverslide. A second cover slip was placed on top, with a droplet of 1.5  $\mu\text{l}$  of immersion oil<sup>3</sup> in between, such as to keep the ambient refractive index constant in the vicinity of the particles.

### Setup

The imaging setup is sketched in Figure 1C. Its basis was formed by a standard dark-field microscope. A confocal aperture in the image plane of the dark-field microscope was used to isolate the scattered light from a single JP. At the other end of the optical path stood a homebuilt spectrograph, consisting of

- an sCMOS camera (pco.edge 4.2) for image acquisition,
- a transmissive diffraction grating (ThorLabs GT125-03A) in front of it, used for spectral dispersal of the image,
- a tunable slit to select only a thin vertical line from an image in order to prevent overlap of spectrally dispersed signals from different points in the original image and
- a lens to propagate the image from the plane of the slit onto the camera sensor.

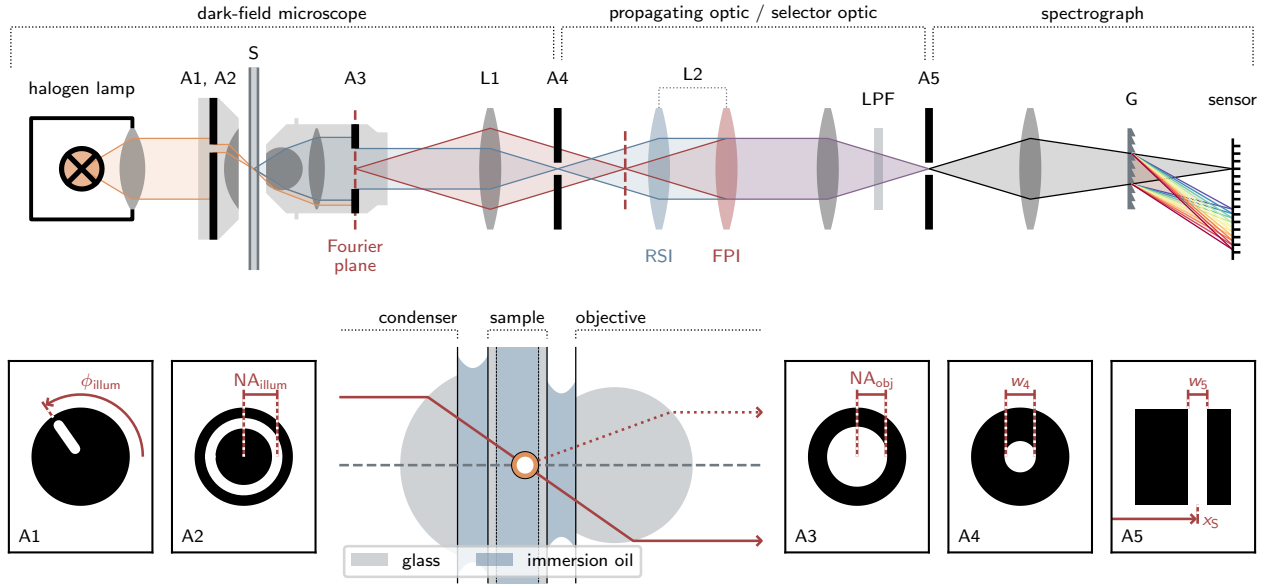


**Figure 1:** Schematics of the imaging optics: **(top)** The dark-field condenser directs the illumination (yellow light path) onto the sample (S); the apertures A1 and A2 restrict the direction of illumination. In the immediate surroundings of the particle under observation **(bottom center)**, the ambient refractive index is virtually homogenous, due to the usage of immersion oil inside the sample. The illuminating light is intercepted by the objective's aperture (A3), while scattered light from objects in the sample is allowed through. The lens L1 produces an image of the sample in the plane of the aperture A4 and an image of the back aperture of the objective (Fourier plane) behind A4, in the plane marked by the red dashed line. The lens L2 can be moved between the real-space imaging (RSI, blue) and the Fourier plane imaging (FPI, red) position, each propagating an image of the corresponding plane onto the slit A5, which functions as the entrance aperture of the spectrograph. Inside the spectrograph, the image from A5 is propagated onto the camera sensor. A diffraction grating produces a spectrally dispersed image, from which spectral data can be read. An optional optical long-pass filter LPF can be used to remove overlap between the first- and second-order

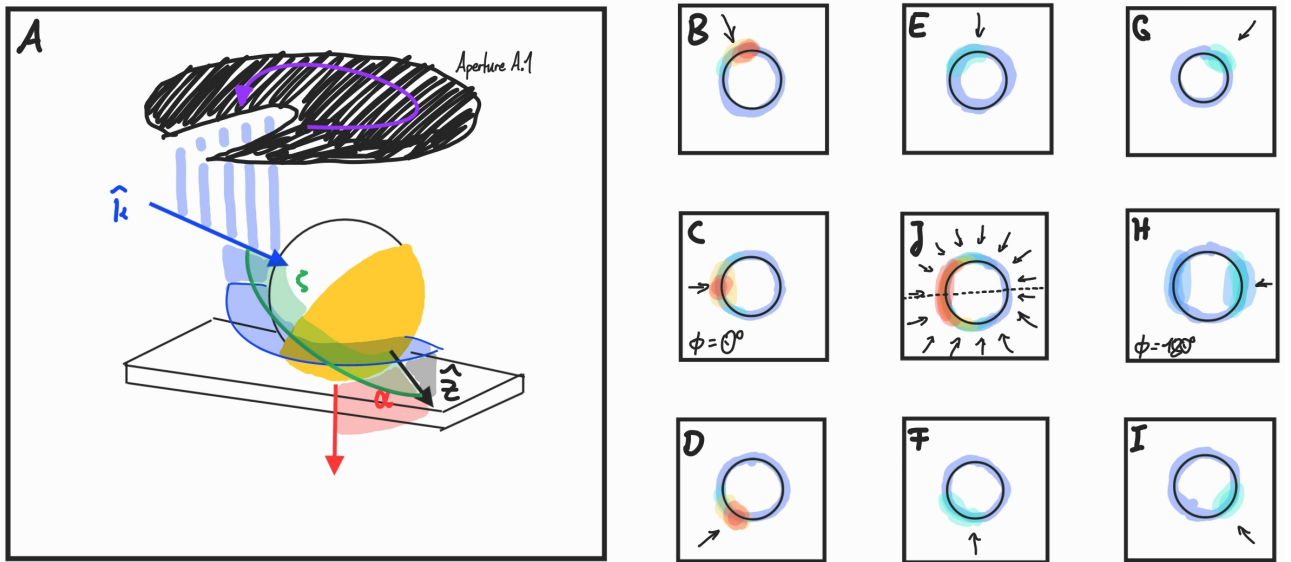


**Figure 2:** Selective Illumination: **A:** By rotating the aperture A.1 the direction of illumination on the particle can be controlled within the range permitted by its out-of-plane orientation. **B-I:** Dark-field images of a JP under restricted illumination. The arrows signify the in-plane angle of the illumination. **J:** The same JP under unrestricted (normal) dark-field illumination.

Both sub-assemblies were linked by a propagating optic, with which either the image plane wherein the aperture lay or the back focal plane (BFP) of the micro-

scope objective could be chosen to be projected onto the slit.

The real-space-imaging mode was used to select

particles for measurement as well as for spectral measurements in which the scattering angle was not resolved. The BFP-imaging mode was used to align the dark-field illumination and to record spectrally resolved Fourier-space images of the JP under observation. To that end, the front aperture of the spectrograph (i.e. the slit) was slowly translated across the BFP image while recording, such that the camera would record one spectrally dispersed vertical line of the BFP image at a time. The accumulation time for one such dataset was approximately 15 minutes.

The calibration data for the wavelength-dependent sensitivity of the optics was collected by allowing the illumination light to pass through the entire assembly and recording its spectrum.

For the samples, a drop of the JP solution was placed on a cover slip and the particles were allowed to sediment for at least 5 minutes. Then, the solvent was blown off the cover slip with compressed air. A second cover slip was placed atop the first one, with a drop ( $\sim 1.5 \mu\text{l}$ ) of immersion oil in between, ensuring no significant changes in the ambient refractive index in the vicinity of the JPs.

## Validation

For validation, the scattering spectra of 65 nm AuNPs were measured. Such small particles were chosen for two reasons: a) The resonance in the expected scattering spectrum would be as narrow as possible and b) the shape of the angular distribution of scattered light would not change appreciably over the spectral range of interest, causing the measured and full scattering cross-sections to only differ by a constant factor. In the comparison of the measured spectra to the predictions of Mie theory [7–9] using the values by Johnson & Christy [10] for the complex refractive index of gold shows a strong agreement.

## Emulation

In order to be able compare the simulation results to the measurements, the limited collection angle of the objective has to be taken into account. Thus, while the "true" scattering intensity is the integral over the angular distribution of scattered light,

$$P_{\text{sca}}(\lambda) = \oint_{S^2} \mathcal{I}(\lambda, \Omega) d\Omega,$$

the measured value corresponds to the integration over a certain angular range  $\mathcal{D} \subset S^2$ .

Essentially, the solver is provided with an analytic expression for the incident electric field  $\vec{E}_{\text{inc}}(\vec{x}, t)$  and returns samples for the scattered field  $\vec{E}_{\text{sca}}(\vec{x}, t)$ , such that the total electric field

$$\vec{E}(\vec{x}, t) = \vec{E}_{\text{inc}}(\vec{x}, t) + \vec{E}_{\text{sca}}(\vec{x}, t)$$

<sup>4</sup>This is allowed because  $I \propto \|\hat{E}\|^2$ .

<sup>5</sup> $p(\alpha)$  is the probability density function for the out-of-plane angle of a randomly oriented spherical JP. For the derivation, see the supplementary material.

satisfies Maxwell's field equations.

For the incident field, a plane wave was given, wherein the illumination angle  $\zeta$  is encoded as a rotation of the incident light field in the  $(x, z)$  plane:

$$\vec{E}_{\text{inc}} = \vec{E}_0 \cdot \exp(i\vec{k} \cdot \vec{x} - i\omega t)$$

with  $\omega = 2\pi c/\lambda$ , as well as

$$\vec{E}_0 = E_0 \cdot \mathbf{R}_k^\chi \cdot \mathbf{R}_y^{\zeta - \frac{\pi}{2}} \cdot \hat{z} \quad \text{and} \quad \vec{k} = \frac{2\pi}{\lambda} \cdot \overbrace{\mathbf{R}_y^\zeta}^{\hat{k}} \cdot \hat{z},$$

where  $\chi$  is the polarisation angle of the incident light field.

The intensity of the incident field is

$$I_0 = \frac{1}{2\mu_0\mu_r} E_0^2.$$

[11, 12]

To emulate the unpolarised light that the measurements were conducted with,  $\chi$  was sampled as  $\in \{0, \pi/2\}$  and, in the evaluation, intensities were averaged.<sup>4</sup>

Through a Fourier transform, the scattered field is decomposed into plane-wave components:

$$\vec{E}_{\text{sca}}(\vec{x}, t) = \iiint_{\mathbb{R}^3} \vec{\mathcal{E}}(\vec{k}) \cdot \exp(i\vec{k} \cdot \vec{x} - i\omega t) d^3\vec{k}.$$

The measured scattering cross-section of the JP corresponds to the sum of the intensities of all plane-wave components of the scattered field that enter the measurement optics:

$$\sigma_{\text{sca,measured}} \propto \iint_{\mathcal{D}} I(\hat{k}') d\Omega,$$

Where  $\mathcal{D} \subseteq S^2$  is the set of propagation directions  $\hat{k}'$ , for which a plane wave component will contribute to the signal on the detector. In the experiment, the requirement is for it to enter the objective, and thus

$$\mathcal{D} = \left\{ \hat{k}' \in S^2 \mid \angle(\hat{k}', \hat{\delta}) < \theta_{\text{NA}} \right\},$$

where  $\theta_{\text{NA}}$  is the opening angle of the objective's collection cone, given by the numerical aperture,

$$\theta_{\text{NA}} = \text{asin} \frac{\text{NA}}{n}.$$

- The simulation provides values of the scattered field for sampled values of  $\zeta$ .
- The numerical aperture of the dark-field condenser defines  $\angle(\hat{k}, \hat{\delta})$ .
- The out-of-plane angle  $\alpha$  of the JP is unknown and not uniquely defined by  $\zeta$  and  $\angle(\hat{k}, \hat{\delta})$ . We sample  $\alpha \in [0, \pi]$  and weight the results by  $p(\alpha) = \sin \alpha$ .<sup>5</sup>

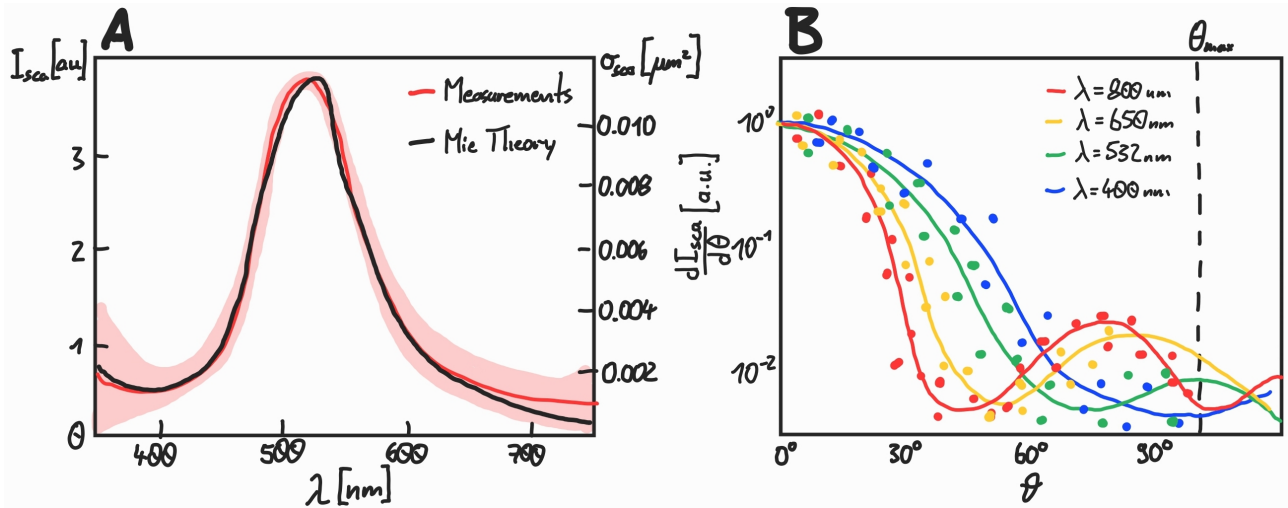


**Figure 3:** (Placeholder) **A:** Scattering spectrum of 65 nm Au NPs. The shaded area corresponds to the SNR. **B:** Scattering intensity of a spherical Au NP,  $d = 250$  nm versus the scattering angle for various wavelengths. The lines show the predictions of GLMT [9], the points show measurement results.

## Results & Discussion

Both the experiment and the simulations show that, in asymmetric cases, light is preferentially scattered in the direction of the Au cap.

The measured intensity increase through the visible range coincides with the increase of the scattering cross-section. In the NIR range, the measured brightness increases further; here it is due to the broadening of the forward scattering peak.

### Global Illumination

[...]

Recorded scattering spectra of the JPs are shown in Figure 4B.

### Orientation Dependent

## Simulation Results

[A summary figure of sim results: scattering spectra, Mie plots and the like]

[We find that the scattering cross-section heavily depends on the orientation of the JP.]

Over the spectral range that we analyzed, though decidedly not in general, the scattering efficiency of the particle was ... greater if it was illuminated from either the Au or the PS side than if it was illuminated side-on. In both cases, the scattering spectra have multiple peaks. Between axial and side-on illumination, though, there is no clear correspondence between these peaks.

E.g., for side-on illumination, there is a scattering peak at  $\lambda \approx 540$  nm, that has no counterpart in the spectra for axial illumination. We ascribe this peak

to the nanostructure plasmon resonance of gold: It sits right around that wavelength and it is only under side-on illumination that the incident electric field may be perpendicular to the surface of the Au cap at its points of highest curvature, that being the cap's perimeter.

The more immediately noticeable feature of the scattering spectra is the pair of peaks at  $\lambda \approx 1000$  nm,<sup>6</sup> which only appears under axial illumination. As  $\hat{k}$  is parallel to the symmetry axis of the JP, the perimeter of the Au cap is coplanar to the electric field and a resonant surface plasmon is excited in it.

Neither of these peaks is present<sup>7</sup> in the scattering spectrum of an equivalently sized Au sphere. This implies that the associated surface plasmon mode is one that does not exist on a closed sphere.

Notable findings are...

- The spectral bump at  $\lambda \approx 550$  nm. It's discernable in both real and emulated measurements, though in the raw simulation data it only appears for side-on illumination. It's likely the same peak as would show up for an arbitrarily small Au NP. The plasmon mode is excited in the rim of the cap by electric fields that are perpendicular to the Au surface at its point(s) of highest curvature. (i.e.  $\vec{E} \parallel \hat{z}$ , which can only happen if  $\hat{k} \perp \hat{z}$ )
- The clearly discernable peak at  $\lambda \approx 1000$  nm is present under the opposite circumstances, i.e. when  $\hat{k} \parallel \hat{z}$ . It corresponds to a surface plasmon resonance of the Au cap. (Polar / Azimuthal?<sup>8</sup>)
- Comparing the angular distributions to those of a Mie particle, there is clear similarity: Non-global maxima become more well-distinguished

<sup>6</sup>precisely, they are at 996.9 nm and 998.9 nm, respectively.

<sup>7</sup>discernable?

<sup>8</sup>Rim modes can, when  $\hat{k} \parallel \hat{z}$ , only really be excited in the fundamental mode. The same should go for azimuthal modes. right?



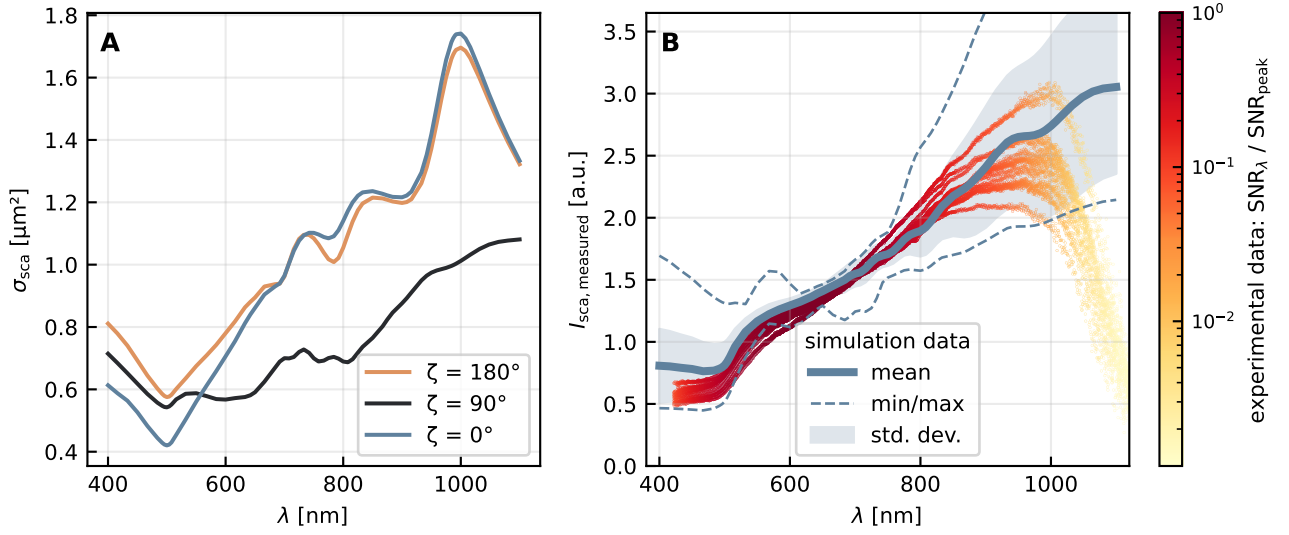


**Figure 4:** **A:** simulated scattering spectrum of the JP under illumination from the Au side (yellow), from the PS side (blue) and from the equatorial side (black). **B:** measured scattering spectra (orange) atop value range as determined by simulation + emulation (blue).

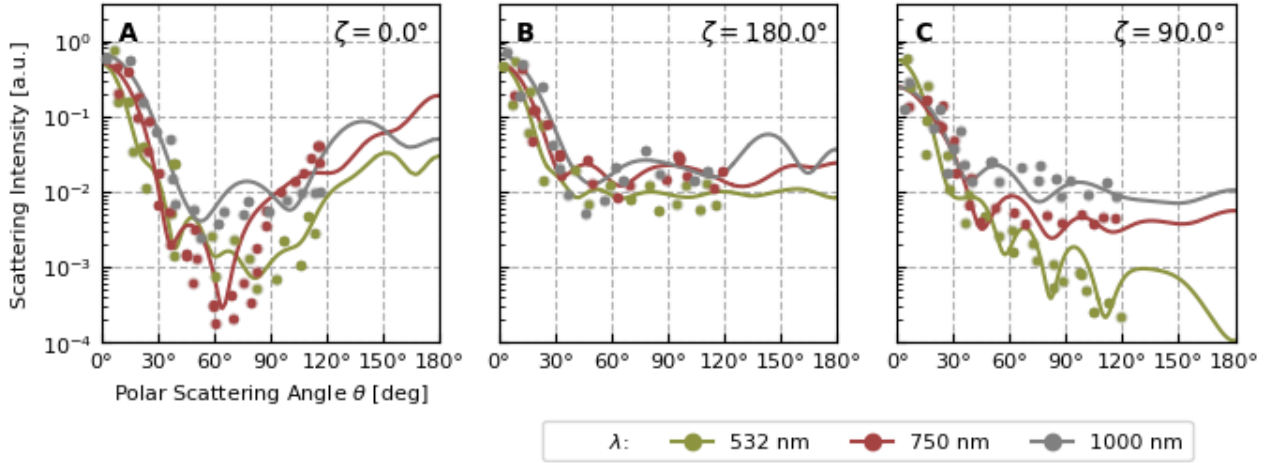


**Figure 5:** Scattering intensity of the JP versus scattering angle. The points signify measured intensities while the lines are simulation results. **A** and **B** show the cylindrically symmetric cases of illumination from the PS side and from the Au side, respectively, i.e. where  $\hat{k} \parallel \hat{z}$ . In **C**, the light is incident side-on ( $\hat{k} \perp \hat{z}$ ,  $\zeta = \pi/2$ ). Disregarding the local extrema, qualitatively distinct large-scale behaviour is apparent: Under illumination from the PS side (**A**), the scattering intensity becomes globally minimal in the sideways direction. Meanwhile, under illumination from the Au side (**B**), it reaches a plateau and under side-on illumination (**C**), the scattering intensity drops consistently between forwards and backwards.

and over-all fewer as wavelength increases. The same happens as the direction of illumination is changed from  $\hat{k} \perp \hat{z}$  to  $\hat{k} \parallel \hat{z}$ : Both transitions can, from a Mie-theoretical point of view, be understood as a decreasing size parameter. (consider the ratio of the effective diameter<sup>9</sup> of the plasmonic structure in the direction of the wave propagation to the wavelength)

- The out-of-plane orientation of the JP is not easy to infer:

It is notable that the bump at  $\lambda \approx 550$  nm that is

<sup>9</sup>“depth”?

discernible in both the real and the emulated measurements ( $\rightarrow$  Fig. 4A), appears in the raw simulation data ( $\rightarrow$  Fig. 4B) only under side-on illumination, i.e.  $\zeta \approx \pi/2$ .

## Conclusion & Outlook

In summary, we conducted spectroscopic studies of the light scattering behaviour of individual, micrometre-sized Janus particles. We find that the anisotropy of the JP causes certain features to appear

in and disappear from its scattering spectrum under certain orientations, particularly in the NIR range.

An experimental setup that can detect these features, possibly even in real time, is feasible.

Interesting things to do with this in the future might be...

- Direct analysis of the surface plasmons: Decomposition of the tangential electric field in an appropriate basis (vector hemispherical harmonics?) to find relative excitation of every (important) surface plasmon mode, depending on wavelength and illumination angle.
- Real-time spectroscopy to track a JP's out-of-plane angle.

## References

1. Bregulla, A. P. & Cichos, F. Flow fields around pinned self-thermophoretic microswimmers under confinement. *J. Chem. Phys.* **151**, 044706. <https://doi.org/10.1063/1.5088131> (2019).
2. Auschra, S., Bregulla, A., Kroy, K. & Cichos, F. Thermotaxis of Janus Particles. *Eur. Phys. J. E* **44**. <https://doi.org/10.1140/epje/s10189-021-00090-1> (2021).
3. Selmke, M., Khadka, U., Bregulla, A. P., Cichos, F. & Yang, H. Theory for controlling individual self-propelled micro-swimmers by photon nudging I: directed transport. *Phys. Chem. Chem. Phys.* **20**, 10502. <https://doi.org/10.1039/c7cp06559k> (2018).
4. Ilic, O. *et al.* Topologically enabled optical nanomotors. *Sci. Adv.* **3**, e1602738. <https://advances.sciencemag.org/content/3/6/e1602738> (2017).
5. Patzschke, F. H. *Finite Elements Simulations of Optical Torques on Metal-Dielectric Janus Particles* Bachelor's Thesis (Universität Leipzig, 2020).
6. Islam, M. M., Hossen, M. M., Koschny, T. & Hillier, A. C. Shape- and Orientation-Dependent Scattering of Isolated Gold Nanostructures Using Polarized Dark-Field Microscopy. *J. Phys. Chem. C* **125**, 11478–11488. eprint: <https://doi.org/10.1021/acs.jpcc.1c03671>. <https://doi.org/10.1021/acs.jpcc.1c03671> (2021).
7. Mie, G. Beiträge zur Optik trüber Medien, speziell kolloidaler Metallösungen. *Annalen der Physik* **330**, 377–445. <https://doi.org/10.1002/andp.19083300302> (3 1908).
8. Bohren, C. F. & Huffman, D. R. *Absorption and Scattering of Light by Small Particles* Wiley Professional Paperback Edition, 82–129, 136. ISBN: 978-0-471-29340-8 (John Wiley & Sons, Weinheim, 1998).
9. Gouesbet, G. & Gréhan, G. *Generalized Lorenz-Mie Theories* Second Edition. ISBN: 978-3-319-46873-0 (Springer, Heidelberg, 2017).
10. Johnson, P. B. & Christy, R. W. Optical Constants of the Noble Metals. *Phys. Rev. B* **6**, 4370. <https://doi.org/10.1103/PhysRevB.6.4370> (1972).
11. Griffiths, D. J. *Introduction to Electrodynamics* Fourth edition. ISBN: 978-0-321-85656-2 (Pearson Education, London, 1981).
12. Patzschke, F. H. *Orientation-dependent Spectroscopy of Plasmonic Janus Particles* Master's Thesis (Universität Leipzig, 2023).

## Acknowledgements

[...]

## Author Contributions

F.C. and F.H.P. designed the experiments; F.H.P. constructed the optical setup, performed the experiments, implemented the simulations and conducted the data analysis; F.H.P. and A.M.A. and wrote the manuscript; All authors reviewed the manuscript.

## Competing Interests

The authors have no competing interests to declare.

## Additional Information

[...]